MATERIALS CHEMISTRY FRONTIERS

RESEARCH ARTICLE

View Article Online
View Journal | View Issue

Cite this: *Mater. Chem. Front.*, 2021, **5**, 5400

In situ grown MnO_2/graphdiyne oxide hybrid 3D nanoflowers for high-performance aqueous zinc-ion batteries†

Fuhui Wang,[ab] Weiyue Jin,[ab] Zecheng Xiong[ab] and Huibiao Liu *[ab]

Manganese dioxide (MnO_2) has been demonstrated to be a promising cathode material for aqueous zinc-ion batteries (ZIBs) due to its low cost, good safety and high output voltage; however, it suffers from an intrinsically low electrical conductivity, poor rate performance and rapid capacity deterioration. Herein, a new kind of MnO_2@GDYO hybrid three-dimensional (3D) nanoflower has been designed and fabricated *via* the *in situ* growth of MnO_2 in graphdiyne oxide (GDYO) nanosheets in aqueous solution. The MnO_2@GDYO hybrid 3D nanoflowers have the dual advantages of MnO_2 and GDYO, which effectively improve the electrochemical activity and reversibility, increase the ion-/electron-transport channels and enhance the structural stability. Meanwhile, the unique 3D nanoflower structure has large specific surface area, shortens the ion-transport distance and improves the electrochemical reaction kinetics. The rechargeable aqueous Zn//MnO_2@50GDYO battery presents an admirable capacity of 253.7 mA h g^{-1} at 1C, a superior rate capacity of 80.6 mA h g^{-1} at 10C, and excellent operating stability over 1000 cycles at 5C with a capacity retention of 77.6% and a coulombic efficiency approaching 100%. The facile preparation and excellent electrochemical performance make hybrid-based graphdiyne oxide a promising candidate as a cathode for high-performance ZIBs.

Received 7th April 2021,
Accepted 18th May 2021

DOI: 10.1039/d1qm00548k

rsc.li/frontiers-materials

Introduction

Rechargeable aqueous zinc-ion batteries (ZIBs) have attracted extensive research activity in recent years because of their resource sustainability, secure electrolyte, simple assembly, eco-friendliness and appreciable energy density.[1,2] The key challenge of ZIBs is to explore suitable cathode materials that possess a high specific capacity, superior rate performance and long-term cycle life, such as manganese-based oxides, vanadium-based oxides and organic compounds.[3,4] Among them, MnO_2 stands out for its high operating potential (approximately 1.4 V *vs.* Zn/Zn^{2+}), large theoretical capacity (308 mA h g^{-1}), inexpensiveness, non-toxicity and easy preparation.[5–7] These virtues make the Zn//MnO_2 system attractive for grid-scale energy-storage deployment. However, the disadvantages of MnO_2 cathodes are their rapid capacity fading, poor rate capability and unsatisfactory cycling stability that arise from their intrinsically poor electrical conductivity, manganese dissolution, phase change and structural damage during repeated discharge–charge processes.[8–10] Therefore, improving the electrochemical activity, inherent stability and suppressing the volumetric change of MnO_2 for a reversible cathode material is an important challenge in aqueous ZIBs based on MnO_2.

There are some strategies for improving the performance of ZIBs based on MnO_2, such as the pre-addition of Mn^{2+} salt in mild aqueous electrolytes for suppressing the dissolution of Mn^{2+} and improving the cycling stability of MnO_2 cathodes,[11,12] developing MnO_2 materials with a vast variety of polymorphs (*i.e.*, α-, β-, γ-, and δ-MnO_2),[13,14] and investigating different morphologies (*i.e.*, nanowires,[15] nanorods,[16] nanospheres[17] and nanoflakes[18]) and their hybrids (*i.e.*, MnO_2/graphene,[19] MnO_2/graphite,[20] MnO_2/carbon nanotube[21] and MnO_2/polyaniline[22]), which have resulted in preliminary achievements. The nanostructural MnO_2 can provide an enlarged electrolyte/electrode contact area, increase the number active sites and shorten ion-/electron-diffusion pathways for promotion of the capacity and reaction kinetics of MnO_2. Various nanostructures of MnO_2 exhibit good electrochemical performances in either batteries or supercapacitors.[23–25] Hybridizing MnO_2 with carbon materials has been considered as an effective approach to improve its electronic conductivity, structural stability and to accommodate the structural change during the cycling process. Various carbon

[a] *Beijing National Laboratory for Molecular Sciences, CAS Research/Education Center for Excellence in Molecular Sciences, CAS Key Laboratory of Organic Solids, Institute of Chemistry, Chinese Academy of Sciences, Beijing 100190, P. R. China. E-mail: liuhb@iccas.ac.cn*

[b] *University of Chinese Academy of Sciences, Beijing 100049, P. R. China*

† Electronic supplementary information (ESI) available. See DOI: 10.1039/d1qm00548k

materials, including graphene, carbon nanotubes and graphite, exhibit superb electrical conductivity when applied in aqueous ZIBs. However, most of the MnO_2/conductive additive composites prepared by physical mixing methods such as ultrasonic mixing,[26] ball milling,[27] and vacuum filtration[28,29] have an obvious phase-separation interface after repeated discharge–charge cycles, which brings about the loss of good conductive contact and internal structure stability. Therefore, it is imperative to introduce new carbon materials and develop new efficient and reliable methods for the preparation of homogeneous hybrid materials based on MnO_2 and novel carbon materials.

Graphdiyne (GDY) is a novel 2D carbon allotrope with benzene rings connected by butadiyne linkages (–C≡C–C≡C–) to form 18-C hexagons and has displayed excellent electrical, catalytic and optical properties.[30–32] The extended existence of sp- and sp^2-hybridized carbon atoms endows GDY with a 2D planar structure, uniformly distributed pores, excellent electrical conductivity, high chemical stability and so on.[33–35] Graphdiyne oxide (GDYO) is one of the important derivatives of GDY, and is prepared by surface oxidation with an oxidizing agent. GDYO preserves the integrity of the skeletal 2D structure of GDY (C≡C, C=C) to ensure a rich pore structure with uniform distribution, and forms abundant hydrophilic oxygen-containing functional groups (C=O) on its basal planes and edges, which are beneficial to guest metal ions, chelating them firmly. Herein, we develop an *in situ* growth strategy to construct MnO_2@GDYO hybrid 3D nanoflowers using GDYO nanosheets. With abundant nanopores in each GDYO skeleton plus the porous network composed of the interconnected GDYO nanosheets, the integrated MnO_2@GDYO hybrid 3D nanoflowers provide numerous channels for the transport of ions/electrons, enhanced charge-transfer kinetics and structural stability. In addition, the 3D nanoflower is capable of greatly enlarging the electrolyte/electrode contact area, increasing the number of active sites and shortening the ion-/electron-diffusion pathways. Furthermore, the size, surface area and morphologies of MnO_2@GDYO hybrid 3D nanoflowers can be tuned by controlling the conditions of *in situ* growth, which results in the controllable performance of aqueous ZIBs. The as-prepared MnO_2@50GDYO hybrid 3D nanoflowers used as a cathode for aqueous ZIBs exhibit a superior rate capability of 80.6 mA h g^{-1} at 10C and an excellent cycling stability of up to 1000 cycles with a capacity retention of 77.6%, a coulombic efficiency approaching 100% and a high capacity of 253.7 mA h g^{-1} at 1C. This work brings new prospects for the design of GDYO hybrids for high-performance rechargeable aqueous ZIBs.

Experimental section

Preparation of GDYO

Graphdiyne (GDY) was synthesized on the surface of copper foil *via* a cross-coupling reaction using hexaethynylbenzene (HEB) precursors as previously described.[30] Graphdiyne oxide (GDYO) was prepared from GDY using a concentrated H_2SO_4/H_2O_2 mixture (volume ratio, 2 : 3) as the oxidizing agent. Briefly, GDY powder (100 mg) was mixed carefully with concentrated H_2SO_4 (1.2 mL) in an ice bath for 10 min. Then hydrogen peroxide (30% H_2O_2, 1.8 mL) was added dropwise into the mixture slowly and stirred vigorously for 12 h at room temperature. For further stripping and oxidation, the mixture was added to distilled water (20 mL) drop by drop under ultrasonication for 4 h. The suspension was centrifuged at 8000 rpm for 5 min and washed several times with distilled water until the supernatant was neutral. Finally, the GDYO powder was obtained by freeze-drying.

Preparation of MnO_2

The synthetic prcedure for MnO_2 is similar to previously reported work.[36] In a typical experiment, 4.0 g of $(NH_4)_2S_2O_8$ was added to 10 mL of H_2O. After vigorous stirring for 20 min, 4.5 g of TMAOH (tetramethylammonium hydroxide, $(CH_3)_4NOH$, 25% wt in H_2O) was added to the mixed solution, followed by stirring for another 20 min and the addition of water to 20 mL, giving a homogeneous solution. The obtained solution was then added to 10 mL of 0.3 M $MnCl_2$ solution slowly over 10 min under vigorous stirring. The dark brown MnO_2 sample was obtained after vigorous stirring overnight in the ambient atmosphere at room temperature. Afterward, the solid sample was collected through vacuum filtration and washed with deionized water and ethanol. Finally, the desired products were obtained after being dried under vacuum at 60 °C. The product was labeled as MnO_2.

Preparation of MnO_2@GDYO hybrid 3D nanoflowers

Firstly, 50 mg of the as-prepared GDYO powder was ultrasonically dispersed in 10 mL of deionized water. Then, 0.3 M $MnCl_2$ was added to the GDYO dispersion solution. After vigorous stirring for 20 min, the $MnCl_2$ was totally dissolved, giving a homogeneous solution. At the same time, 4.0 g of $(NH_4)_2S_2O_8$ was added to another 10 mL of H_2O. After vigorous stirring for 20 min, 4.5 g of TMAOH was added to the mixed solution, followed by another 20 min of stirring and the addition of water to 20 mL. The above solution was then added to the GDYO dispersion solution containing 0.3 M $MnCl_2$ slowly over 10 min under vigorous stirring. The dark brown MnO_2@GDYO hybrid 3D nanoflowers were obtained after vigorous stirring overnight in the ambient atmosphere at room temperature. The product was vacuum filtered, washed three times with deionized water and ethanol, and thoroughly dried under vacuum at 60 °C. The product was labeled as MnO_2@50GDYO. Different ratio MnO_2@GDYO hybrids were synthesized *via* controlling the mass of the GDYO in the mixtures, where the MnO_2@GDYO hybrids with GDYO loadings of 10 mg, 20 mg and 100 mg are named MnO_2@10GDYO, MnO_2@20GDYO and MnO_2@100GDYO, respectively.

Material characterization

Scanning electron microscope (SEM) images were collected using a Hitachi S-4800 microscope, combined with energy dispersive X-ray spectroscopy (EDS) for the determination of elemental composition. Transmission electron microscopy (TEM), high-resolution transmission electron microscopy (HR-TEM) images and elemental mapping results were

obtained using a JEM-2100F electron microscope operating at 200 kV. X-Ray diffraction (XRD) measurement was performed using a Japan Rigaku D/max-2500 rotation anode X-ray diffractometer and graphite-monochromated Cu Kα radiation (λ = 1.54178 Å) with a scan rate of 5° min^{-1} from 5° to 90° (2θ). Raman spectra were recorded using an NT-MDT NTEGRA Spectra system, with excitation from an Ar laser at 473 nm. X-Ray photoelectron spectroscopy (XPS) was performed using a VG Scientific ESCALab220i-XL X-ray photoelectron spectrometer, with Mg or Al Kα radiation as the excitation source. Thermogravimetric analysis (TGA) was carried out using Mettler-Toledo TGA/SDTA851 apparatus under a flow of air at a heating rate of 5 °C min^{-1} from 30 to 800 °C. Nitrogen adsorption and desorption measurements were performed using a Micromeritics ASAP 2020HD88 model instrument (Norcross, GA, USA). The specific surface area of the hybrids were determined using the Brunauer–Emmett–Teller (BET) method.

Preparation of cathode electrodes

To prepare the cathodes, the synthesized MnO_2 and MnO_2@GDYO hybrid 3D nanoflowers (70 wt%) were mixed with a conductive additive (carbon black, 20 wt%) and a binder (polyvinylidene fluoride, PVDF, 10 wt%) in a solvent of *N*-methyl-2-pyrrolidone (NMP), respectively, mixing with constant stirring until a homogeneous slurry was obtained. Next, the resulting slurry was cast onto Ti foils using the doctor blading method and dried under vacuum at 80 °C for 6 h. Finally, the electrodes were cut into round discs with a diameter of 10 mm for further use. The average mass loading of the active materials was about 1 mg cm^{-2}.

Electrochemical characterization

Zinc foil and filter paper were used as the anode and separator, respectively, and 2 M $ZnSO_4$ with 0.1 M $MnSO_4$ additive solution was employed as the electrolyte. CR 2032-type coin cells were assembled in air to evaluate the electrochemical performance. Cyclic voltammetry (CV) and electrochemical impedance spectroscopy (EIS) were measured using a CHI 660E electrochemical workstation. The electrochemical properties, including the specific capacity, rate capacity and cycling performance, were evaluated using the galvanostatic charge–discharge method on a LAND battery testing system (Land CT 2001A) at different current densities. All tests were carried out at room temperature.

Results and discussion

The MnO_2@GDYO hybrid 3D nanoflowers were prepared through an *in situ* induced growth strategy. Briefly, the homogeneous $(NH_4)_2S_2O_8$ and $(CH_3)_4NOH$ aqueous solution was dripped into $MnCl_2$ aqueous solution containing uniformly dispersed GDYO nanosheets in aqueous solution. The mixture reacted under constant vigorous stirring at room temperature for 12 hours. The MnO_2@GDYO hybrid 3D nanoflowers were obtained after washing and drying (details are in the Experimental section). The size, surface area and morphologies of the MnO_2@GDYO hybrid 3D nanoflowers can be tuned by controlling the conditions of *in situ* growth. The growth process of the MnO_2@GDYO hybrid 3D nanoflowers is proposed as depicted in Fig. 1. The Mn^{2+} species were anchored on the surface of the GDYO nanosheets (Fig. S1, ESI†) through their carboxyl groups in the mixed solution. After the addition of $(NH_4)_2S_2O_8$ and $(CH_3)_4NOH$ aqueous solution, the MnO_2 nuclei began to be formed on the surface of GDYO nanosheets and grew in size. Subsequently, 2D MnO_2 nanosheets gradually formed under the induction of the GDYO nanosheets. Then, the obtained 2D MnO_2 nanosheets crosslinked with the GDYO nanosheets through the carboxyl functional groups of GDYO to produce the MnO_2@GDYO hybrid 3D nanoflowers. In this *in situ* growth process, the amount of GDYO nanosheets is a key factor for the size, surface area and morphology of the MnO_2@GDYO hybrid 3D nanoflowers. An excess of GDYO nanosheets promotes the agglomeration of 3D nanoflowers, while a lack of GDYO nanosheets results in a hybrid material with a low degree of cross-linking, and only an appropriate amount of GDYO nanosheets can induce 3D nanoflowers with a perfect structure.

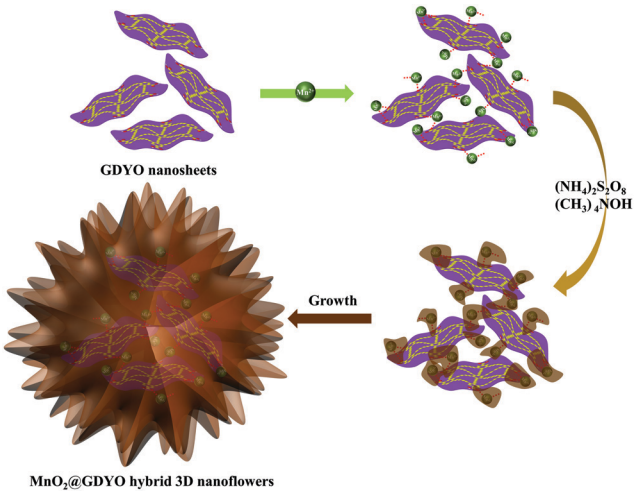

Fig. 1 Schematic illustration of the formation of the MnO_2@GDYO hybrid 3D nanoflowers.

The morphology and structure of the MnO_2@GDYO hybrid 3D nanoflowers were characterized by SEM and TEM (Fig. 2 and Fig. S2–S4, ESI†). From the SEM images, the evolution of the MnO_2@GDYO nanostructures indicates that the morphologies are well controlled. With an increase in the amount of GDYO, the formation of thinner and finer 3D nanoflower structures of MnO_2@GDYO hybrids are promoted compared with bare MnO_2 (Fig. S5, ESI†). Fig. 2 shows the typical morphology of MnO_2@50GDYO, which is composed of agglomerated nanoflowers with ample wrinkles and folds. There was no obvious exposure of GDYO nanosheets, which confirmed that all MnO_2 grew on the surface of GDYO, covering it completely, and there was no separated phase interface as illustrated in Fig. S6 (ESI†). Such an interconnected network not only ensures the electrochemical activity but also enhances the integral mechanical stability. More detailed structural information can be obtained by TEM, and all of the MnO_2@GDYO hybrids display a thin sheet-like morphology which folds up into complex 3D

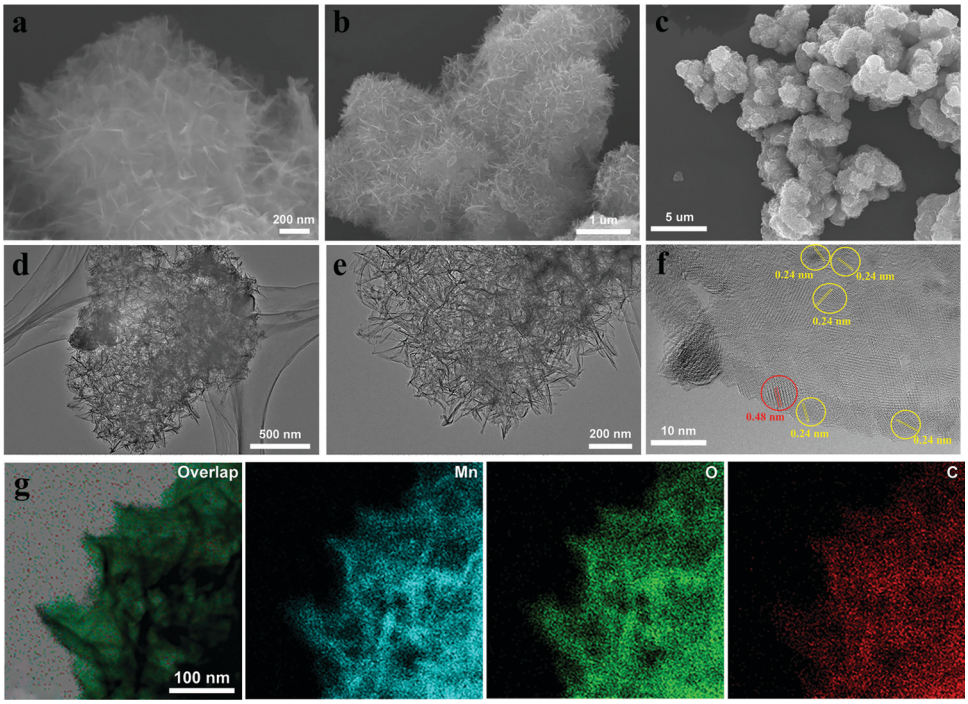

Fig. 2 Microstructural and compositional analysis of the MnO_2@50GDYO hybrid 3D nanoflowers: (a–c) SEM images; (d and e) TEM images; (f) HR-TEM image; and (g) elemental mapping images of Mn, O and C.

nanoflower structures. When the content of GDYO is too low, the morphology of the MnO_2@10GDYO hybrid is close to that of MnO_2, which has a thicker and larger sheet aggregated structure. With the increase of GDYO content, the degree of cross-linking between MnO_2 and GDYO increases, gradually forming the ultra-thin sheet aggregate structure. However, when the amount of GDYO is too high, the MnO_2@100GDYO hybrid aggregates severely, covering the exposed surface of the ultrafine structure, and resulting in a decrease in the specific surface area and pore structure. The TEM images of the MnO_2@50GDYO hybrid indicate that the flower-like structures are constructed from nanosheets, consistent with the SEM observations. High-resolution TEM (HR-TEM) characterization of the MnO_2@50GDYO hybrid is shown in Fig. 2f, and the lattice spacings of 0.24 nm and 0.48 nm are found to match well with the (006) and (004) crystal planes, respectively, of birnessite-MnO_2. Moreover, energy dispersive X-ray spectroscopy (EDS) mapping images (Fig. 2g) with respect to Mn, O and C show that these elements are abundant and well-distributed throughout the nanoflower, suggesting that the MnO_2 grows uniformly on the GDYO surface. Similar results were obtained in the MnO_2@10GDYO, MnO_2@20GDYO, and MnO_2@100GDYO hybrids.

The crystallographic structures of the MnO_2@GDYO hybrid 3D nanoflowers were confirmed by XRD. As shown in Fig. 3a and Fig. S7 (ESI†), all of the diffraction peaks can be well indexed to pure phase birnessite-MnO_2 (JCPDS 18-0802) and GDYO. The peaks at 12.1°, 24.7°, 36.5°, 53.2° and 65.6° are related to the (002), (004), (006), (301) and (119) planes of birnessite-MnO_2, respectively. GDYO exhibits a broad diffraction peak around 23°, which is ascribed to the typical interlayer distance of the GDY material.[37,38] In addition, the XRD patterns for the MnO_2@GDYO hybrid 3D nanoflowers present less noticeable peaks for MnO_2 and a high peak for GDYO, showing the combination of MnO_2 and GDYO. It is noticeable that the peaks with a broad feature and low intensity are indicative of the nanoscale structure and low crystallinity of the MnO_2@GDYO hybrid 3D nanoflowers, which is in line with the HR-TEM observations. In particular, when the GDYO content reached 100 mg, the corresponding (002) and (004) diffraction peaks in the XRD pattern almost disappeared, and the lattice spacing of 0.48 nm was not observed in the HR-TEM image (Fig. S4f, ESI†).

To further characterize the composites, Raman analysis was carried out. As shown in Fig. 3b and Fig. S8 (ESI†), a sharp peak is seen at 648 cm^{-1}, which can be attributed to the symmetric Mn–O stretching vibrations of the MnO_6 octahedron in MnO_2, similar to those previously reported.[39] In addition, in the spectrum of the MnO_2@GDYO hybrid 3D nanoflowers, the prominent peaks of GDYO are seen at 1378 and 1589 cm^{-1}, corresponding to the defect-induced (D band) and graphitic-induced (G band) carbon structures, respectively, demonstrating the presence of MnO_2 and GDYO.

XPS measurement was carried out to investigate the chemical composition and the electronic states of the MnO_2 and MnO_2@GDYO hybrid 3D nanoflowers. The existence of elemental C, O, and Mn signals are obvious from the full-scan XPS spectrum (Fig. 3c), suggesting the presence of manganese oxide and carbon materials. The C 1s peak of the MnO_2@50GDYO hybrid 3D nanoflowers can be deconvoluted into four subpeaks of

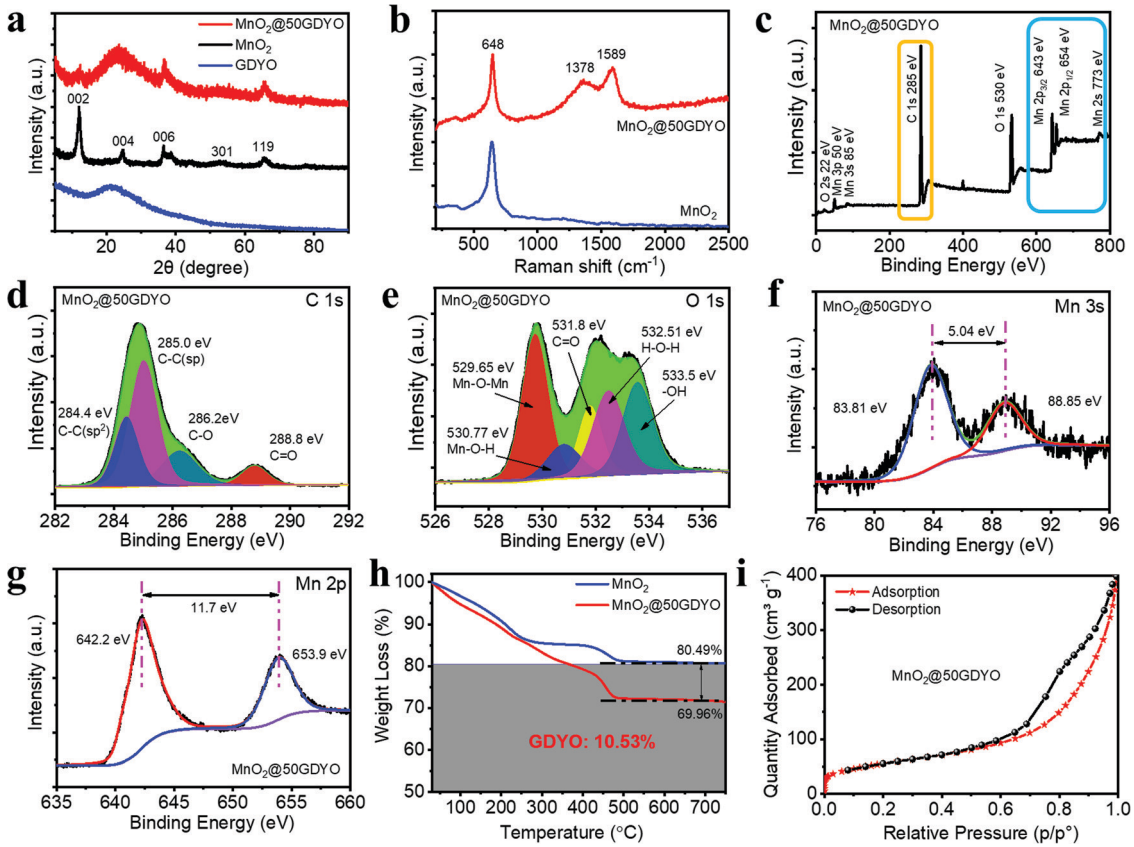

Fig. 3 Characterization of the MnO_2@50GDYO hybrid 3D nanoflowers. (a) XRD patterns. (b) Raman spectra. XPS spectra: (c) survey scan, and (d–g) narrow scan for elements C, O, and Mn. (h) TGA curves. (i) Nitrogen adsorption–desorption isotherm at 77 K.

C=C (sp^2), C≡C (sp), C–O, and C=O at 284.4, 285.0, 286.2, and 288.8 eV, respectively (Fig. 3d), consistent with the expected chemical composition of GDYO.[40] The deconvoluted O 1s spectrum shows that five components appear at 529.65, 530.77, 531.8, 532.51 and 533.5 eV (Fig. 3e), which are in turn indexed to Mn–O–Mn bonds for the tetravalent oxide, Mn–O–H bonds for a hydrated trivalent oxide, C=O bonds for the carboxyl groups on the surface of GDYO, H–O–H bonds for residual water and –OH bonds for the hydroxyl groups on the surface of GDYO, respectively. The peak splitting of the doublet in the Mn 3s core-level spectrum is about 5.04 eV, suggesting that Mn^{4+} is dominant in the MnO_2@50GDYO hybrid 3D nanoflowers. Moreover, the shoulder peaks of Mn 2p in Fig. 3g are characteristic of Mn $2p_{1/2}$ (653.9 eV) and Mn $2p_{3/2}$ (642.2 eV), agreeing well with the typical spin energy separation of 11.7 eV for MnO_2.[41] The same results for MnO_2@10GDYO, MnO_2@20GDYO and MnO_2@100GDYO have been obtained and are presented in Fig. S9 (ESI†). The results clearly confirm that the MnO_2@GDYO hybrid 3D nanoflowers were successfully prepared.

TGA was used to study the content of GDYO in the MnO_2@GDYO hybrid 3D nanoflowers (Fig. 3h and Fig. S10, ESI†). The weight loss below 240 °C is derived from the removal of adsorbed water, and the subsequent decrease originates from the combustion of GDYO to CO_2.[16] For MnO_2, a weight loss of about 5% is observed in the range of 240–500 °C, which is attributed to the phase transformation of MnO_2.[42] By calculation, we estimated that the mass percentage of GDYO in the MnO_2@50GDYO hybrid 3D nanoflowers is about 10.53%. The results for the GDYO mass percentage obtained in the MnO_2@10GDYO, MnO_2@20GDYO and MnO_2@100GDYO hybrid 3D nanoflowers are about 3.79%, 5.91%, 16.92%, respectively.

Fig. 3i shows the nitrogen adsorption–desorption isotherm of the MnO_2@50GDYO hybrid 3D nanoflowers, in which the remarkable hysteresis loop in the intermediate P/P_0 range illustrates a unique mesoporous texture and the BET specific surface area is as high as 204.83 $m^2\ g^{-1}$, exceeding that of the pure MnO_2 (77.93 $m^2\ g^{-1}$). The measured value is higher than those reported for MnO_2 prepared using other synthetic routes (Table S1, ESI†). The samples with different GDYO contents all showed similar hysteresis loops with mesoporous dominant structural characteristics, and the BET specific surface areas are calculated as 81.85 (MnO_2@10GDYO), 130.53 (MnO_2@20GDYO), and 128.30 $m^2\ g^{-1}$ (MnO_2@100GDYO) (Fig. S11 and S12, ESI†). In particular, the use of excessive GDYO resulted in agglomeration, a smaller specific surface area and a larger volume expansion for MnO_2@100GDYO (Fig. S13, ESI†). It is believed that the mesoporous architecture and the large specific surface area of MnO_2 can not only promote the swift diffusion, transportation, and intercalation of electrolyte ions throughout the electrode, but also accommodate the volume change of MnO_2 during the charging–discharging processes.[43]

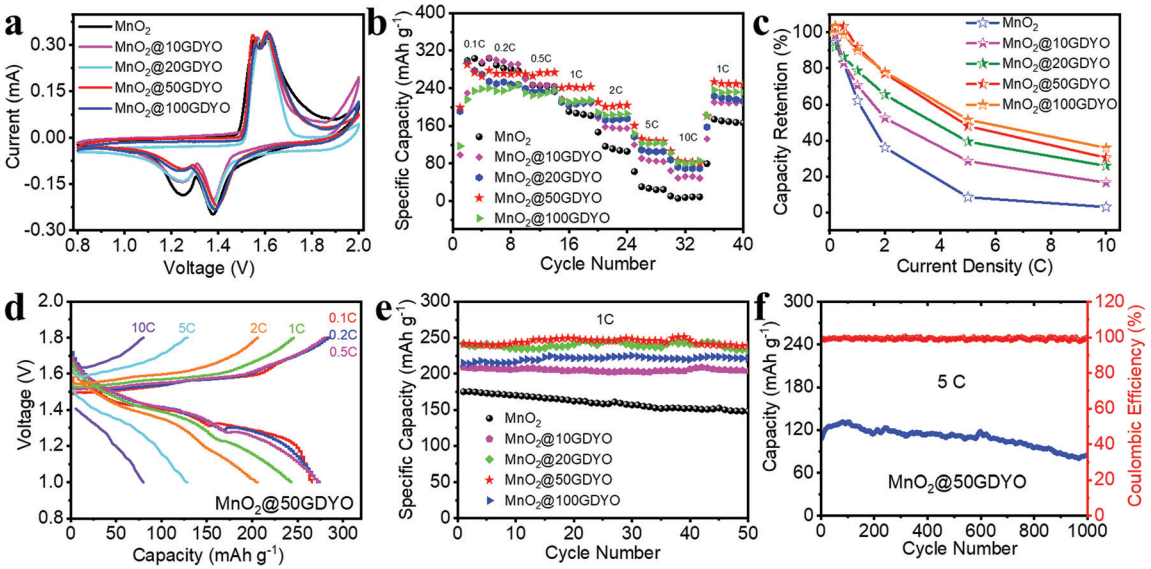

Fig. 4 Electrochemical performance of the MnO_2@GDYO hybrid 3D nanoflowers. (a) CV curves at 0.1 mV s^{-1}. (b) Rate performance. (c) Capacity retention. (d) Charge and discharge curves of the MnO_2@50GDYO electrode at current densities ranging from 0.1 to 10C. (e) Cycle performance at 1C (1C = 308 mA h g^{-1}) in the voltage of 1–1.8 V after the rate performance test. (f) Long-term cycling performance of the MnO_2@50GDYO electrode at 5C.

To investigate the electrochemical performance of the MnO_2@GDYO hybrid 3D nanoflowers as a cathode for aqueous ZIBs, coin-type cells were assembled using Zn foil as the anode. Fig. 4a exhibits the CV curves of MnO_2 and MnO_2@GDYO electrodes at a scan rate of 0.1 mV s^{-1}. There are two couples of redox reactions, indicating that the ZIBs undergo a two-step electrochemical process. It should be noted that GDYO makes no capacity contribution to zinc ion storage as shown in Fig. S14a and b (ESI†). Fig. 4b presents the rate performances tested at different current densities, and corresponding cycle profiles are given in Fig. 4d and Fig. S14c–f (ESI†). In addition to MnO_2@100GDYO, MnO_2 and other MnO_2@GDYO electrodes have an approximate specific capacity at 0.1C, indicating that the excess GDYO actually reduces the specific capacity of the battery. Although MnO_2@100GDYO cathode makes a higher capacity retention rate, it comes at the cost of specific capacity. In the process of developing electrode materials, the specific capacity should be considered as well as the rate performance. When the GDYO amount is increased to 50 mg, both the specific capacity and the rate capability stand out among the five samples. Therefore, the optimized hybrid MnO_2@50GDYO is used for the following study. As shown in Fig. 4b, the MnO_2@50GDYO cathode delivers the capacities of 265.1, 272.3, 273.8, 243.0, 204.3, 127.4, and 80.6 mA h g^{-1} at discharge–charge rates of 0.1, 0.2, 0.5, 1, 2, 5 and 10C (based on the active mass of MnO_2), respectively. More importantly, when the current rate switches back to 1C, the capacity recovers to 253.7 mA h g^{-1}, which is 95.7% of the value at 0.1C. The high-rate capability is not only superior to the corresponding values for the control electrodes as displayed in Fig. 4c, but is also comparable to those of known MnO_2 cathode materials reported previously (Table S2, ESI†). This outstanding rate performance can be understood based on the EIS results of MnO_2 and MnO_2@GDYO electrodes, and the resulting Nyquist plots were fitted by the inset equivalent circuit (Fig. S15a, ESI†). The high frequency semi-circle corresponds to the charge-transfer resistance (R_{ct}), the low-frequency inclined line stands for the Warburg impedance (Z_w) and R_0 is the series resistance of the electrochemical system. The detailed EIS information is shown in Table S3 (ESI†). According to the results, the MnO_2@GDYO electrodes exhibit significantly smaller R_0 and R_{ct} values, and a lower Warburg diffusion resistance (the steeper slope). As a consequence, the introduction of the GDYO in the *in situ* grown MnO_2 can effectively enhance the charge-transfer ability, and thereby accelerate the electrode reaction kinetics for a high rate performance. The excellent rate performance also can be attributed to the 3D flower-like MnO_2@GDYO nanostructures, which provide a high specific surface area for more active sites and a unique mesoporous nanotexture for ion-diffusion channels as well as the porous nature of GDYO. The specific capacity could return to the initial level when the current density is switched back to a current rate of 1C, again confirming the high reactivity and reversibility of the MnO_2@GDYO cathodes. In addition to the excellent rate capability, the MnO_2@GDYO cathodes also possesses remarkable cyclability. Fig. 4e compares the cycling performance of MnO_2 and MnO_2@GDYO cathodes at 1C. Dramatic capacity fading can be clearly observed from the cycling curves of MnO_2 in the initial cycles. The MnO_2@GDYO cathodes all have an excellent cycle stability, but the presence of excessive GDYO will reduce its specific capacity, for example, the specific capacity of MnO_2@100GDYO hybrid is only 215 mA h g^{-1} at 1C. The higher specific capacity of the MnO_2@GDYO cathodes is due to the larger specific surface area and higher number of active sites of the MnO_2@GDYO hybrid 3D nanoflower material. Serious aggregation of MnO_2@100GDYO hybrid leads to a decrease in specific surface area, which in turn leads to a decrease in the specific capacity. The structural stability of

the MnO_2@GDYO cathodes was strengthened by the ingenious *in situ* induction growth strategy, and the cycling and rate properties of the MnO_2@GDYO cathodes were significantly improved. Of the five electrodes, the MnO_2@50GDYO hybrid clearly exhibits the best cycling performance (239 mA h g^{-1} after 50 cycles, a capacity retention ratio of 99.2% at 1C), even after cycling for over 150 cycles (Fig. S16, ESI†). The long-term cycling stability with quite a high current density of 5C over 1000 cycles shows a remarkable capacity retention of 77.6% and coulombic efficiency approaching 100% (Fig. 4f). After the discharge–charge testing, postmortem analysis shows that the electrode retains the nanoflower morphology, indicating the strong structural stability of the MnO_2@GDYO hybrids (Fig. S17, ESI†).

The fundamental energy-storage mechanism of the MnO_2@GDYO cathodes, using MnO_2@50GDYO as an example, during electrochemical cycling is investigated by *ex situ* XRD, SEM and XPS measurements to unveil the phase and microstructural evolution. Fig. 5a shows the typical charge–discharge curves for the initial two cycles marked with different states from A to I. During the initial discharging (A–B–C), the corresponding XRD patterns exhibit diffraction peaks at 19° and 35°, which belong to MnOOH (JPCDS 18-0804) (Fig. 5b and Fig. S18, ESI†), formed because of the reaction of proton insertion into manganese dioxide, $H^+ + MnO_2 + e^- \rightarrow MnOOH$. The gradual depletion of H^+ would lead to an enrichment of OH^- surrounding the cathode and thus the subsequent OH^- react with $ZnSO_4$ and H_2O in the aqueous electrolyte, $6OH^- + 4Zn^{2+} + SO_4^{2-} + 3H_2O \rightarrow Zn_4SO_4(OH)_6{\cdot}3H_2O$.[44–46] From this, a new phase with characteristic 2θ peaks at around 10°, 21°, 22°, 26°, 28°, and 59° appear in the discharge plateau, which can be assigned to zinc sulfate hydroxide hydrate ($Zn_4SO_4(OH)_6{\cdot}3H_2O$, JPCDS 39-0689). With deep discharging to 1.0 V (C and G), the peak intensity of $Zn_4SO_4(OH)_6{\cdot}3H_2O$ increases, indicating the growth of the

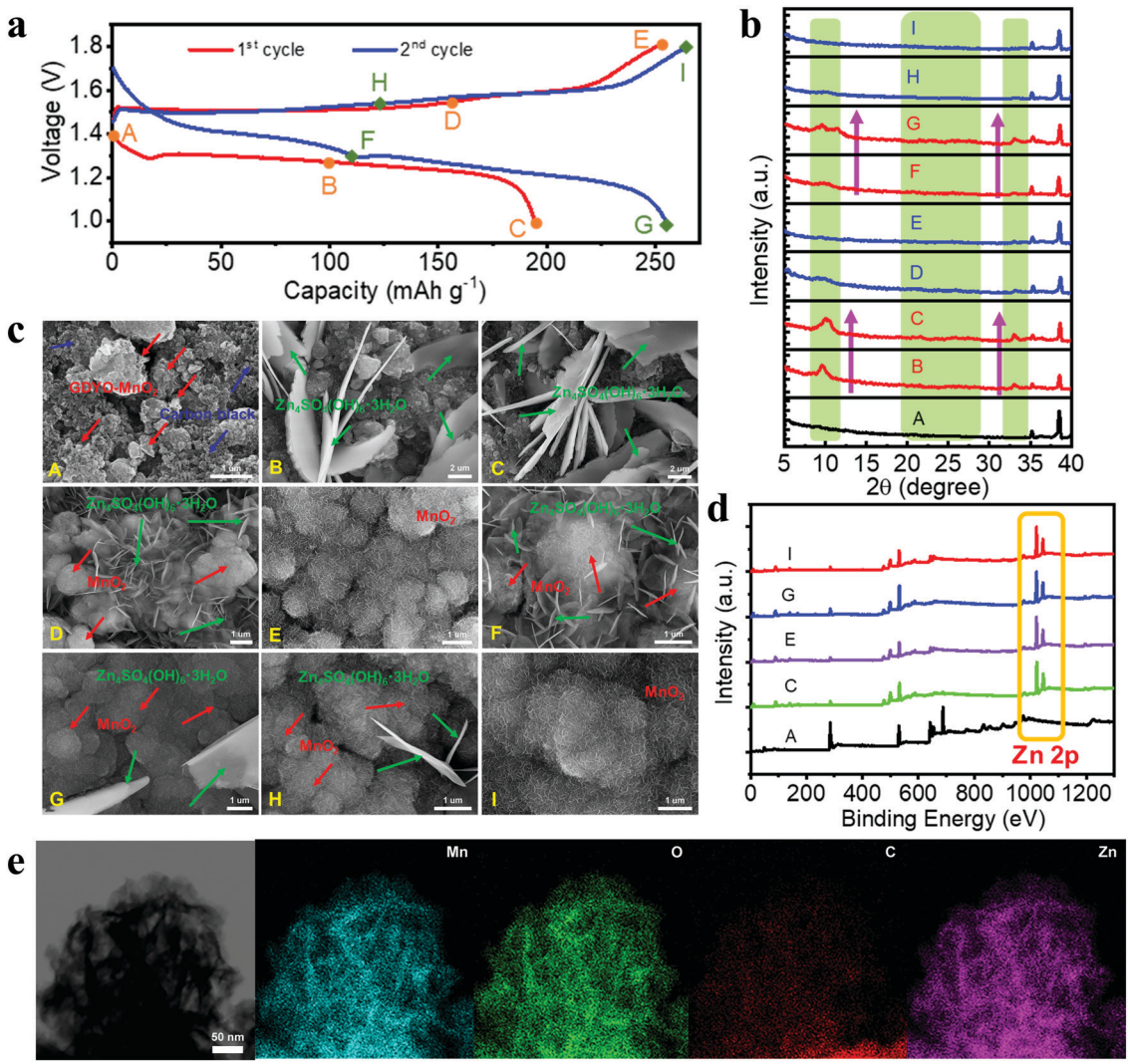

Fig. 5 Energy-storage mechanism of the MnO_2@50GDYO cathode. (a) Typical charge–discharge curves for the initial two cycles at 1C. (b) XRD patterns. (c) SEM images. (d) XPS surveys collected at various states marked in (a). (e) The elemental mapping images of Mn, O, C and Zn for the MnO_2@50GDYO cathode after cycling.

$Zn_4SO_4(OH)_6{\cdot}3H_2O$ structure. As displayed in Fig. 5c and Fig. S18 (ESI†), the ultrathin nanosheets evolve into large size micro-sheets and a white substance can be observed on the electrode surface. Compared with the original state, a new diffraction peak emerges at 33°, which depicts the formation of $ZnMn_2O_4$ (JCPDS 24-1133). This can be attributed to the insertion of Zn^{2+} into the MnO_2 tunnels, accompanied by the valence decrease of positive quadrivalent manganese (Fig. 5d and Fig. S19, ESI†), $Zn^{2+} + 2MnO_2 + 2e^- \rightarrow ZnMn_2O_4$. HR-TEM EDS mapping of the MnO_2@50GDYO cathode in a fully discharged state offers further proof of the insertion of Zn^{2+}, while the Zn signal is seen uniformly everywhere (Fig. 5e). In the reverse charging process (C–D–E, G–H–I), the extraction of H^+ and Zn^{2+} from the electrode could result in the dissolution of the $Zn_4SO_4(OH)_6{\cdot}3H_2O$ phase. Both the diffraction peaks of the $Zn_4SO_4(OH)_6{\cdot}3H_2O$ phase and the micro-sheets disappear, revealing a reversible precipitation–dissolution of the $Zn_4SO_4(OH)_6{\cdot}3H_2O$ structure. A reversible precipitation–dissolution process can be maintained even after long-term cycle testing, as shown in Fig. S20 (ESI†). Therefore, the energy-storage mechanism is a co-insertion/extraction process of Zn^{2+} and H^+ into MnO_2 accompanied by the precipitation–dissolution of the $Zn_4SO_4(OH)_6{\cdot}3H_2O$ phase.

Conclusions

In summary, a novel *in situ* induced growth strategy has been developed to construct 3D nanoflower MnO_2@GDYO hybrids, which not only have the advantages of the 2D GDYO porous structure but also show characteristics of the 3D nanostructure. The combined properties of large surface area, enhanced charge-transfer kinetics and superior structural integrity are achieved in the MnO_2@GDYO hybrid 3D nanoflowers. The MnO_2@GDYO hybrid 3D nanoflowers have been fabricated as cathodes in aqueous ZIBs. The aqueous ZIBs of MnO_2@50GDYO exhibit a high reversible capacity of 265.1 mA h g^{-1} at 0.1C, an excellent rate capability of 253.7 mA h g^{-1} at 1C and 80.6 mA h g^{-1} at 10C, and decent cycling stability over 1000 cycles at 5C (with a capacity retention of 77.6% and a coulombic efficiency approaching 100%). The results demonstrate a novel perspective and idea on constructing advanced hybrid materials for high-performance aqueous zinc-ion batteries.

Conflicts of interest

There are no conflicts to declare.

Acknowledgements

This study was supported by the National Key Research and Development Project of China (2016YFA0200104 and 2018YFA0703501) and the National Nature Science Foundation of China (21790050, 21790053, 21875258, 22071251).

References

1 Y. C. Shi, Y. Chen, L. Shi, K. Wang, B. Wang, L. Li, Y. M. Ma, Y. H. Li, Z. H. Sun, W. Ali and S. J. Ding, An overview and future perspectives of rechargeable zinc batteries, *Small*, 2020, **16**, 2000730.
2 X. H. Zeng, J. N. Hao, Z. J. Wang, J. F. Mao and Z. P. Guo, Recent progress and perspectives on aqueous Zn-based rechargeable batteries with mild aqueous electrolytes, *Energy Storage Mater.*, 2019, **20**, 410–437.
3 Y. L. Zhao, Y. H. Zhu and X. B. Zhang, Challenges and perspectives for manganese-based oxides for advanced aqueous zinc-ion batteries, *InfoMat*, 2020, **2**, 237–260.
4 L. E. Blanc, D. Kundu and L. F. Nazar, Scientific challenges for the implementation of Zn-ion batteries, *Joule*, 2020, **4**, 1–29.
5 X. Y. Liu, J. Yi, K. Wu, Y. Jiang, Y. Y. Liu, B. Zhao, W. L. Li and J. J. Zhang, Rechargeable Zn-MnO_2 batteries: Advances, challenges and perspectives, *Nanotechnology*, 2020, **31**, 122001.
6 J. F. Li, Y. H. Chen, J. Guo, F. H. Wang, H. B. Liu and Y. L. Li, Graphdiyne oxide-based high-performance rechargeable aqueous Zn-MnO_2 battery, *Adv. Funct. Mater.*, 2020, **30**, 2004115.
7 D. L. Chao, W. H. Zhou, C. Ye, Q. H. Zhang, Y. G. Chen, L. Gu, K. Davey and S. Z. Qiao, An electrolytic Zn-MnO_2 battery demonstrated for high-voltage and scalable energy storage, *Angew. Chem., Int. Ed.*, 2019, **59**, 7823–7828.
8 G. Z. Fang, C. Y. Zhu, M. H. Chen, J. Zhou, B. Y. Tang, X. X. Cao, X. S. Zheng, A. Q. Pan and S. Q. Liang, Suppressing manganese dissolution in potassium manganate with rich oxygen defects engaged high-energy-density and durable aqueous zinc-ion battery, *Adv. Funct. Mater.*, 2019, **29**, 1808375.
9 M. Li, Q. He, Z. L. Li, Q. Li, Y. X. Zhang, J. S. Meng, X. Liu, S. D. Li, B. K. Wu, L. N. Chen, Z. A. Liu, W. Luo, C. H. Han and L. Q. Mai, A novel dendrite-free Mn^{2+}/Zn^{2+} hybrid battery with 2.3 V voltage window and 11000-cycle lifespan, *Adv. Energy Mater.*, 2019, **9**, 1901469.
10 D. L. Chao, C. Ye, F. X. Xie, W. H. Zhou, Q. H. Zhang, Q. F. Gu, K. Davey, L. Gu and S. Z. Qiao, Atomic engineering catalyzed MnO_2 electrolysis kinetics for a hybrid aqueous battery with high power and energy density, *Adv. Mater.*, 2020, **32**, 2001894.
11 M. Chamoun, W. R. Brant, C. W. Tai, G. Karlsson and D. Noréus, Rechargeability of aqueous sulfate Zn/MnO_2 batteries enhanced by accessible Mn^{2+} ions, *Energy Storage Mater.*, 2018, **15**, 351–360.
12 C. X. Xie, T. Y. Li, C. Z. Deng, Y. Song, H. M. Zhang and X. F. Li, A highly reversible neutral zinc/manganese battery for stationary energy storage, *Energy Environ. Sci.*, 2020, **13**, 135–143.
13 M. Song, H. Tan, D. L. Chao and H. J. Fan, Recent advances in Zn-ion batteries, *Adv. Funct. Mater.*, 2018, **28**, 1802564.
14 B. K. Wu, G. B. Zhang, M. Y. Yan, T. F. Xiong, P. He, L. He, X. Xu and L. Q. Mai, Graphene scroll-coated alpha-MnO_2

nanowires as high-performance cathode materials for aqueous Zn-ion battery, *Small*, 2018, **14**, 1703850.

15 J. J. Wang, J. G. Wang, X. P. Qin, Y. Wang, Z. Y. You, H. Y. Liu and M. H. Shao, Superfine MnO_2 nanowires with rich defects toward boosted zinc ion storage performance, *ACS Appl. Mater. Interfaces*, 2020, **12**, 34949–34958.

16 C. Wang, Y. X. Zeng, X. Xiao, S. J. Wu, G. B. Zhong, K. Q. Xu, Z. F. Wei, W. Su and X. H. Lu, γ-MnO_2 nanorods/graphene composite as efficient cathode for advanced rechargeable aqueous zinc-ion battery, *J. Energy Chem.*, 2020, **43**, 182–187.

17 J. J. Wang, J. G. Wang, H. Y. Liu, C. G. Wei and F. Y. Kang, Zinc ion stabilized MnO_2 nanospheres for high capacity and long lifespan aqueous zinc-ion batteries, *J. Mater. Chem. A*, 2019, **7**, 13727–13735.

18 Y. Zhang, S. J. Deng, Y. H. Li, B. Liu, G. X. Pan, Q. Liu, X. L. Wang, X. H. Xia and J. P. Tu, Anchoring MnO_2 on nitrogen-doped porous carbon nanosheets as flexible arrays cathodes for advanced rechargeable Zn-MnO_2 batteries, *Energy Storage Mater.*, 2020, **29**, 52–59.

19 J. J. Wang, J. G. Wang, H. Y. Liu, Z. Y. You, Z. Li, F. Y. Kang and B. Q. Wei, A highly flexible and lightweight MnO_2/Graphene membrane for superior zinc-ion batteries, *Adv. Funct. Mater.*, 2020, **31**, 2007397.

20 R. L. Liang, J. Fu, Y. P. Deng, Y. Pei, M. W. Zhang, A. P. Yu and Z. W. Chen, Parasitic electrodeposition in Zn-MnO_2 batteries and its suppression for prolonged cyclability, *Energy Storage Mater.*, 2020, **36**, 478–484.

21 S. Bi, Y. Wu, A. Cao, J. Tian, S. Zhang and Z. Niu, Free-standing three-dimensional carbon nanotubes/amorphous MnO_2 cathodes for aqueous zinc-ion batteries with superior rate performance, *Mater. Today Energy*, 2020, **18**, 100548.

22 J. H. Huang, Z. Wang, M. Y. Hou, X. L. Dong, Y. Liu, Y. G. Wang and Y. Y. Xia, Polyaniline-intercalated manganese dioxide nanolayers as a high-performance cathode material for an aqueous zinc-ion battery, *Nat. Commun.*, 2018, **9**, 2906.

23 Q. L. Wei, F. Y. Xiong, S. S. Tan, L. Huang, E. H. Lan, B. Dunn and L. Q. Mai, Porous one-dimensional nanomaterials: design, fabrication and applications in electrochemical energy storage, *Adv. Mater.*, 2017, **29**, 1602300.

24 H. Luo, B. Wang, F. D. Wu, J. H. Jian, K. Yang, F. Jin, B. W. Cong, Y. Ning, Y. Zhou, D. L. Wang, H. K. Liu and S. X. Dou, Synergistic nanostructure and heterointerface design propelled ultra-efficient *in situ* self-transformation of zinc-ion battery cathodes with favorable kinetics, *Nano Energy*, 2021, **81**, 105601.

25 R. X. Fei, H. W. Wang, Q. Wang, R. Y. Qiu, S. S. Tang, R. Wang, B. B. He, Y. S. Gong and H. J. Fan, In situ hard-template synthesis of hollow bowl-like carbon: a potential versatile platform for sodium and zinc ion capacitors, *Adv. Energy Mater.*, 2020, **10**, 2002741.

26 C. Y. Wang, M. Q. Wang, Z. C. He, L. Liu and Y. D. Huang, Rechargeable aqueous zinc-manganese dioxide/graphene batteries with high rate capability and large capacity, *ACS Appl. Energy Mater.*, 2020, **3**, 1742–1748.

27 J. Cao, D. D. Zhang, X. Y. Zhang, S. M. Wang, J. T. Han, Y. S. Zhao, Y. H. Huang and J. Q. Qin, Mechanochemical reactions of MnO_2 and graphite nanosheets as a durable zinc ion battery cathode, *Appl. Surf. Sci.*, 2020, **534**, 147630.

28 Y. Huang, Z. X. Li, S. Y. Jin, S. D. Zhang, H. L. Wang, P. Hiralal, Gehan A.J. Amaratunga and H. Zhou, Carbon nanohorns/nanotubes: An effective binary conductive additive in the cathode of high energy-density zinc-ion rechargeable batteries, *Carbon*, 2020, **167**, 431–438.

29 D. S. Li, Q. L. Gao, H. Zhang, Y. F. Wang, W. L. Liu, M. M. Ren, F. G. Kong, S. J. Wang and J. Chang, MnO_2 particles grown on the surface of N-doped hollow porous carbon nanospheres for aqueous rechargeable zinc ion batteries, *Appl. Surf. Sci.*, 2020, **510**, 145458.

30 G. X. Li, Y. L. Li, H. B. Liu, Y. B. Guo, Y. J. Li and D. B. Zhu, Architecture of graphdiyne nanoscale films, *Chem. Commun.*, 2010, **46**, 3256–3258.

31 Y. R. Xue, B. L. Huang, Y. P. Yi, Y. Guo, Z. C. Zuo, Y. J. Li, Z. Y. Jia, H. B. Liu and Y. L. Li, Anchoring zero valence single atoms of nickel and iron on graphdiyne for hydrogen evolution, *Nat. Commun.*, 2018, **9**, 1460.

32 C. S. Huang, Y. J. Li, N. Wang, Y. R. Xue, Z. C. Zuo, H. B. Liu and Y. L. Li, Progress in research into 2D graphdiyne-based materials, *Chem. Rev.*, 2018, **118**, 7744–7803.

33 Y. H. Chen, J. F. Li, F. H. Wang, J. Guo, T. G. Jiu, H. B. Liu and Y. L. Li, Chemical modification: Toward solubility and processability of graphdiyne, *Nano Energy*, 2019, **64**, 103932.

34 Z. Y. Jia, Y. J. Li, Z. C. Zuo, H. B. Liu, C. S. Huang and Y. L. Li, Synthesis and Properties of 2D Carbon-Graphdiyne, *Acc. Chem. Res.*, 2017, **50**, 2470–2478.

35 J. F. Li, C. J. Wan, C. Wang, H. Zhang and X. D. Chen, 2D material chemistry: Graphdiyne-based biochemical sensing, *Chem. Res. Chin. Univ.*, 2020, **36**, 622–630.

36 X. Peng, Y. Q. Guo, Q. Yin, J. C. Wu, J. Y. Zhao, C. M. Wang, S. Tao, W. S. Chu, C. Z. Wu and Y. Xie, Double-exchange effect in two-dimensional MnO_2 nanomaterials, *J. Am. Chem. Soc.*, 2017, **139**, 5242–5248.

37 H. Shang, Z. C. Zuo, H. Y. Zheng, K. Li, Z. Y. Tu, Y. P. Yi, H. B. Liu, Y. J. Li and Y. L. Li, N-doped graphdiyne for high-performance electrochemical electrodes, *Nano Energy*, 2018, **44**, 144–154.

38 H. B. Liu, J. Guo, M. Y. Guo, F. H. Wang, W. Y. Jin, C. Y. Chen and Y. L. Li, Graphdiyne:A new structure of fluorescent quantum dots, *Angew. Chem., Int. Ed.*, 2020, **59**, 16712–16716.

39 J. Xu, J. Q. Li, Q. L. Yang, Y. Xiong and C. G. Chen, *In situ* synthesis of MnO_2@graphdiyne oxides nanocomposite with enhanced performance of supercapacitors, *Electrochim. Acta*, 2017, **251**, 672–680.

40 J. Li, X. Gao, Z. Z. Li, J. H. Wang, L. Zhu, C. Yin, Y. Wang, X. B. Li, Z. F. Liu, J. Zhang, C. H. Tung and L. Z. Wu, Superhydrophilic graphdiyne accelerates interfacial mass/electron transportation to boost electrocatalytic and photoelectrocatalytic water oxidation activity, *Adv. Funct. Mater.*, 2019, **29**, 1808079.

41 W. P. Fan, W. B. Bu, B. Shen, Q. J. He, Z. W. Cui, Y. Y. Liu, X. P. Zheng, K. L. Zhao and J. L. Shi, Intelligent MnO_2 nanosheets anchored with upconversion nanoprobes for

concurrent pH-/H_2O_2-responsive UCL imaging and oxygen-elevated synergetic therapy, *Adv. Mater.*, 2015, **27**, 4155–4161.

42 N. Palaniyandy, M. A. Kebede, K. Raju, K. I. Ozoemena, L. le Roux, M. K. Mathe and R. Jayaprakasam, α-MnO_2 nanorod/onion-like carbon composite cathode material for aqueous zinc-ion battery, *Mater. Chem. Phys.*, 2019, **230**, 258–266.

43 H. H. Sun, J. G. Wang, Y. Zhang, W. Hua, Y. Y. Li and H. Y. Liu, Ultrafast lithium energy storage enabled by interfacial construction of interlayer-expanded MoS_2/N-doped carbon nanowires, *J. Mater. Chem. A*, 2018, **6**, 13419–13427.

44 H. L. Pan, Y. Y. Shao, P. F. Yan, Y. W. Cheng, K. S. Han, Z. M. Nie, C. M. Wang, J. H. Yang, X. L. Li, P. Bhattacharya, K. T. Mueller and J. Liu, Reversible aqueous zinc/manganese oxide energy storage from conversion reactions, *Nat. Energy*, 2016, **1**, 16039.

45 I. Stosevski, A. Bonakdarpour, F. Cuadra and D. P. Wilkinson, Highly crystalline ramsdellite as a cathode material for near-neutral aqueous MnO_2/Zn batteries, *Chem. Commun.*, 2019, **55**, 2082–2085.

46 Y. Li, S. Y. Wang, J. R. Salvador, J. P. Wu, B. Liu, W. L. Yang, J. Yang, W. Q. Zhang, J. Liu and J. H. Yang, Reaction mechanisms for long-life rechargeable Zn/MnO_2 Batteries, *Chem. Mater.*, 2019, **31**, 2036–2047.